International Journal of Multiphase Flow 165 (2023) 104475

Contents lists available at ScienceDirect

International Journal of Multiphase Flow

journal homepage: www.elsevier.com/locate/ijmulflow

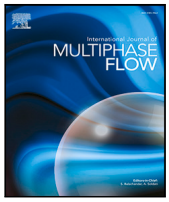

Regimes of the length of a laminar liquid jet fragmented by a gas co-flow

Nathanaël Machicoane [a,*], Rodrigo Osuna-Orozco [b], Alberto Aliseda [b]

[a] Univ. Grenoble Alpes, CNRS, Grenoble INP, LEGI, 38000 Grenoble, France
[b] University of Washington, Department of Mechanical Engineering, Seattle, WA 98105, USA

ARTICLE INFO

Keywords:
Atomization
Coaxial two-fluid atomizer
Spray
Fragmentation
Liquid core length
High-speed imaging

ABSTRACT

Atomization occurs when a high-speed gas jet breaks a low-speed liquid jet coaxial to it, forming a spray via the production of ligaments, sheets, and drops. This mechanism has received a lot of attention and different fragmentation regimes have been identified qualitatively using imaging in the vicinity of the nozzle's exit plane, as a proxy for the change of underlying break-up mechanisms. As the Weber number increases, i.e. as the gas aerodynamic stresses become larger with respect to the liquid surface tension, the liquid–gas interface suffers from instabilities that are governed by either capillarity, shear, or acceleration (or a combination of these). Several fragmentation regimes, in the low Weber number range, are typically deemed undesirable for applications such as propulsion or additive manufacturing, but no quantitative regime map is readily available. Using back-lit high-speed imaging in a multiscale approach, coaxial two-fluid fragmentation is studied in a broad range of gas Weber numbers that spans five fragmentation regimes. A fixed laminar liquid injection rate is maintained while the gas jet exit velocity is varied widely. The liquid core length, i.e. the extent of the liquid jet that is still fully connected to the nozzle, is an important metric of fragmentation, but most research has been focused on its average value in the bag break-up and fiber-type atomization regimes. The scaling laws of the first three statistical moments, the minimum value, and the correlation time of the liquid core length are reported across fragmentation regimes. The changes in scaling laws appear to be good indicators for several of the transitions explored.

1. Introduction

Liquid fragmentation is ubiquitous in nature and industry, with examples ranging from sea sprays over the ocean to powder production for additive manufacturing (Villermaux, 2007). The simplest fragmentation experiment consists of the discharge of a liquid jet from a circular orifice into an ambient atmosphere. Past a certain injection rate, a sustained water jet is observed, unlike dripping found at lower velocities (Clanet and Lasheras, 1999), and the jet suffers from the well-known Rayleigh–Plateau instability. When the liquid jet velocity is further increased, the shear between the high-speed liquid and the stagnant ambient gas dominates the break-up, producing broader drop size distributions in what is referred to as the first wind-induced regime. At even higher velocities, the onset of turbulence in the liquid jet produces small-scale corrugations in the vicinity of the nozzle exit, and contributes together with the aerodynamic forces to fragmentation in the second wind-induced regime, before a transition to liquid atomization, where drops much smaller than the liquid jet diameter are peeled off the liquid jet and a spray is produced. When characterizing changes in fragmentation regimes as the liquid jet velocity increases, one can refer to a stability curve, shown in Fig. 1. The latter represents the evolution of the average length of the liquid jet until break-up with the velocity, along the various regimes. This length, sometimes called intact length or break-up length, is referred to here as liquid core length and represents the contiguous portion of the liquid jet, i.e. the length of the jet that is still connected to the nozzle. An exhaustive list of references concerning the subsequent regimes of the stability curve can be found in Dumouchel (2008). The different regimes are characterized by different scalings for this length, which allows for clear quantitative distinctions. Note that the behavior in the liquid atomization regime, or pressure atomization, which is reached for large values of the liquid velocity and injection pressure, is not sketched as it is out of the scope of this contribution. In this regime, the stability curve is heavily influenced by the geometry of the nozzle and its internal flow (e.g. level of turbulence and cavitation).

This paper aims at applying to coaxial two-fluid atomization the concept of one or more stability curves from the fragmentation of a liquid jet into a still atmosphere. In the latter, alternatively known as gas-assisted atomization, the liquid jet fragmentation is due to a high-speed annular gas jet that surrounds the liquid. Coaxial atomization also presents several break-up regimes (Chigier and Farago,

* Corresponding author.
E-mail address: nathanael.machicoane@univ-grenoble-alpes.fr (N. Machicoane).

https://doi.org/10.1016/j.ijmultiphaseflow.2023.104475
Received 17 December 2022; Received in revised form 7 March 2023; Accepted 7 April 2023
Available online 22 April 2023

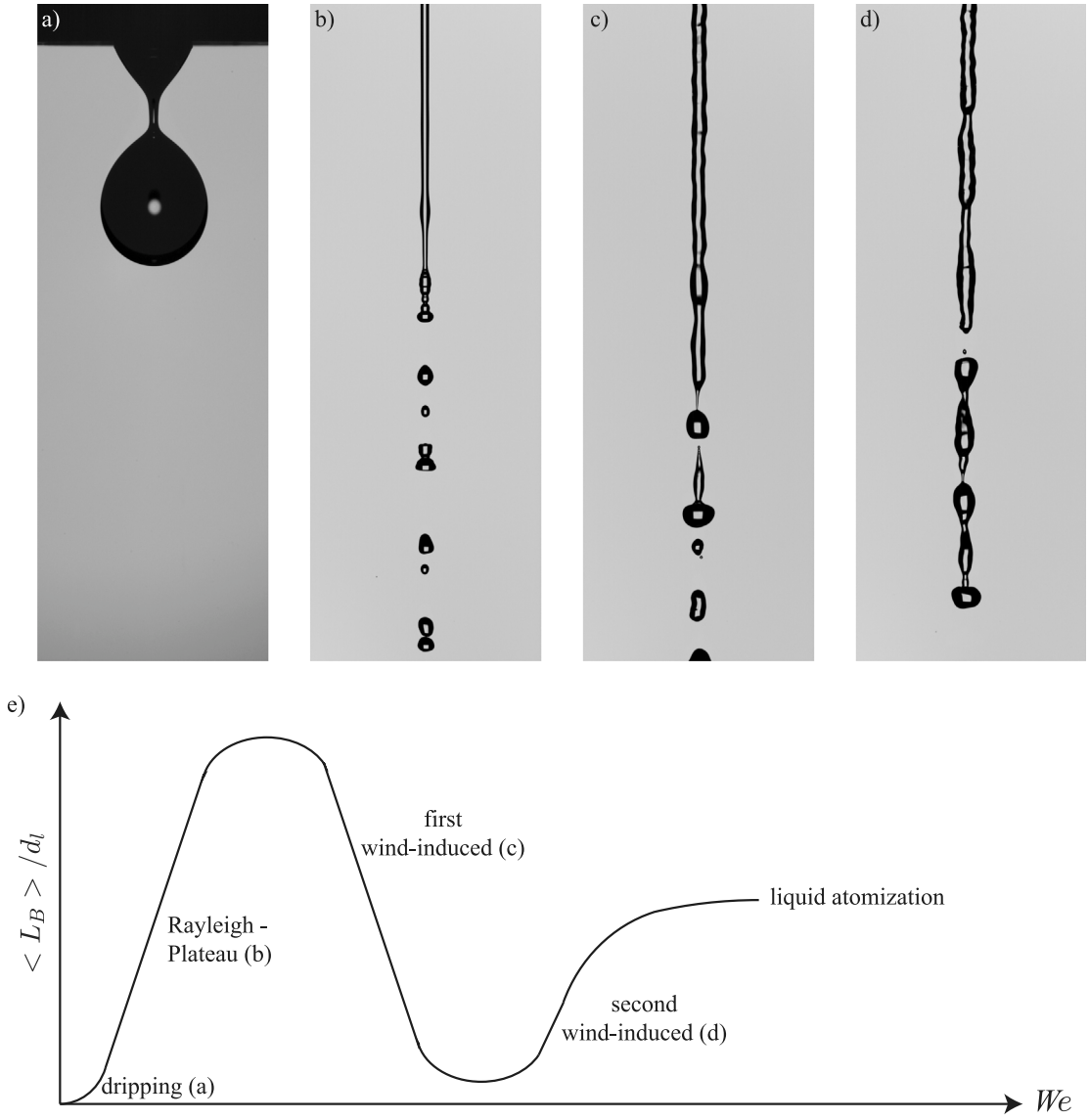

Fig. 1. Visualizations of the fragmentation of a liquid jet discharged into a stagnant gas in the dripping (a), Rayleigh–Plateau (b), first wind-induced (c), and second wind-induced (d) regimes. (e) Schematic stability curve relating the average liquid core length $\langle L_B \rangle$ to the Weber number We, increased from (a) to (d) by increasing the liquid flow rate here. d_l corresponds the liquid nozzle inner diameter.

1992; Lasheras and Hopfinger, 2000), which, when reported in a liquid Reynolds number and gas Weber number parameter space, partly overlap with the stability curve of pressure atomization. The gas Weber number is defined here to compare the liquid jet's surface tension force d_l/σ, where d_l is the liquid nozzle inner diameter and σ the surface tension, to the gas jet aerodynamic stresses $\rho_g U_g^2$, where ρ_g is the gas density and U_g the average exit velocity of the gas jet. For low enough liquid Reynolds number (laminar liquid injection), at zero gas velocity, Rayleigh–Plateau break-up is observed. When the gas velocity increases, break-up is almost identical but the axisymmetry is lost, giving the name to the non-axisymmetric Rayleigh–Plateau break-up regime (see Fig. 3 for illustrations of this and the subsequent fragmentation regimes in coaxial atomization). This is followed by the shear-break-up regime, where the velocity difference between the gas and liquid phase gives rise to a meandering motion of the liquid jet called flapping (Eroglu et al., 1991; Juniper and Candel, 2003; Mayer and Branam, 2004; Charalampous et al., 2009; Delon et al., 2018; Kaczmarek et al., 2022), which dominates break-up here. The liquid jet is bent in arcs that stretch and form long and thin ligaments that exhibit capillary instabilities. At higher gas Weber numbers, the gas can flatten the liquid jet, especially in transverse portions created by the bends, and stretch the liquid into thin membranes called bags. This type of shear break-up is hence referred to as bag break-up, and produces very small droplets issued from the membranes, while the bags' rims fragment into larger drops. A further increase of the gas Weber number gives rise to a succession of Kelvin–Helmholtz and Rayleigh–Taylor instabilities at the gas–liquid interface (Varga et al., 2003; Marmottant and Villermaux, 2004; Aliseda et al., 2008; Matas et al., 2018), forming ligaments that are stripped from the liquid jet. This produces very small droplets and is referred to as the fiber-type atomization regime.

Among these regimes, atomization is typically defined as conditions where the most probable droplets formed are much smaller than the liquid jet diameter (e.g. 50 μm or less for a millimetric jet), and where such droplets are at least partially produced close to the atomizer exit from primary break-up events (directly issued from the liquid jet) (Osuna-Orozco et al., 2022). This is the case in the bag-break-up and fiber-type atomization regimes. For these conditions, the liquid core length has been studied in depth, starting in the early 1990s' (Eroglu et al., 1991). However, as can be seen in comprehensive studies spanning a wide range of operating parameters (Leroux et al.,

2007), no effect from the change in atomization regimes is displayed on the liquid core length: the average value presents a monotonic decrease, with a constant power law of exponent around −0.3 with respect to the gas-to-liquid dynamic pressure ratio M (Leroux et al., 2007; Zhao et al., 2014; Kumar and Sahu, 2020). The latter is defined as $M = \rho_g U_g^2/\rho_l U_l^2$, where ρ_l is the liquid density, and has been shown to control the average liquid core length. Recent work has focused on a deeper analysis of the liquid core length, encompassing its statistics and temporal dynamics Kumar and Sahu (2018), Charalampous et al. (2019), Machicoane et al. (2020), Singh et al. (2021), Kaczmarek et al. (2022), Fong et al. (2022). The goal of this paper is to leverage these approaches to develop a quantitative framework that identifies the signature of changes in coaxial atomization regimes. Such changes play key roles in the droplet size distributions and in the spray dispersion regimes further downstream (Huck et al., 2022). The experimental set-up, measurements and analysis methods are presented in Sections 2 and 3. Section 4 presents the framework and its results in identifying regimes, which is followed by a discussion and conclusions (Sections 5 and 6).

2. Experimental setup and measurements

The coaxial two-fluid atomizer described in Machicoane et al. (2019) is used for this study (Fig. 2). Water is injected through a 100-mm long pipe, reaching fully developed laminar Poiseuille flow. The mean exit velocity is fixed at $U_l = 0.53$ m/s, yielding a liquid Reynolds number $Re_l = U_l d_l/\nu_l \approx 1200$, with d_l the liquid nozzle inner diameter and ν_l the kinematic viscosity of water. The liquid nozzle is centered in the axisymmetric nozzle, where gas is injected through 4 ports, and exits through an annular cross-section of area $A_g = \pi(d_g^2 - D_l^2)/4$, where D_l is the inner diameter and d_g the outer diameter. The gas volumetric flow rate exiting the nozzle Q_g is used to define a gas mean exit velocity and a gas Reynolds number, as $U_g = Q_g/A_g$ and $Re_g = 4Q_g/\sqrt{4\pi A_g}\nu_g$, where ν_g is the kinematic viscosity of air. The interactions between the liquid and gas phases can be described using alternatively the gas-to-liquid dynamic pressure ratio $M = \rho_g U_g^2/\rho_l U_l^2$ or the gas Weber number based on the liquid jet We_{d_l}. The latter is introduced using the velocity difference between the average exit velocities of each of the phases, with $We_{d_l} = \rho_g(U_g - U_l)^2 d_l/\sigma$, following the definition of Lasheras and Hopfinger (2000). The gas Weber number will be used in this paper as it represents well the qualitative transitions in fragmentation regimes (Lasheras and Hopfinger, 2000). At a fixed liquid velocity, varying the gas velocity from 0 to 138 m/s results in maximal values of Re_g, M, and We_{d_l} of respectively 8.7 10^4, 83, and 621. In addition, Table 1 provides reference values of the non-dimensional parameters that are representative of the study. Note that the nozzle is vertical and the longitudinal axis x is aligned with gravity.

Over 20 operating conditions are explored in this study, spanning the various fragmentation regimes described above. Time series of L_B are acquired using high-speed back-lit imaging, following the procedure described in Machicoane et al. (2020), where on each frame the liquid core length represents the downstream extent of the jet that is still connected to the nozzle, projected along the spray's axis x. To compensate for the large variations in the liquid core length average values $\langle L_B \rangle$, 4 optical magnifications are used (achieved by changing the lens or the working distance to the experiment), resulting in different fields of view (represented at scale in Fig. 2). This yields a reduced spatial resolution when the magnification decreases as the number of pixels and their physical size are fixed. However, as the average liquid core lengths increases as M (equivalently We_{d_l}) decreases, the two-phase flow presents larger spatial and temporal scales. The temporal resolution is also adapted accordingly as the magnifications are changed. The resulting ranges of fields of view, spatial and temporal resolutions are reported in Table 2. Due to hardware limitations, the temporal resolution is relatively lower for high gas velocity conditions than for lower ones, resulting in a sparser temporal sampling. It remains sufficient for the computation of correlation times, as at least a dozen points are present before decorrelation for every condition. In addition, the exposure time is always low, ranging from 1 to 10 μs, and no motion blur is observed. Finally, over 12 000 frames were captured, ensuring more than 100 uncorrelated measurements of L_B for each condition, which result in a convergence error of about respectively 2, 5, and 10% on its mean, standard deviation, and skewness (see Kaczmarek et al. (2022)).

Table 1
Flow parameters for fixed laminar liquid injection ($U_l = 0.53$ m/s, $Re_l \simeq 1200$), varying the total gas flow rate in the conditions of Fig. 3(a–j). The gas velocity is $U_g = Q_g/A_g$, the gas Reynolds number is $Re_g = 4Q_g/\sqrt{4\pi A_g}\nu_g$, the gas-to-liquid momentum ratio is $M = \rho_g U_g^2/\rho_l U_l^2$, and the gas Weber number is based on the liquid diameter as $We_{d_l} = \rho_g(U_g - U_l)^2 d_l/\sigma$. The fluids are air and distilled water, at an ambient temperature of 25 °C, with kinematic viscosities of $\nu_g = 1.56\ 10^{-5}$ m^2 s^{-1} and $\nu_l = 8.96\ 10^{-7}$ m^2 s^{-1}, densities $\rho_g = 1.18$ kg m^{-3} and $\rho_l = 996.9$ kg m^{-3}, and the air–water surface tension $\sigma = 72$ mN m^{-1}.

U_g (m/s)	Re_g	M	We_{d_l}
0	0	0	0.01
8	4 800	0.26	1.7
11	6 600	0.48	3.3
15	9 500	1	7.1
19	12 000	1.5	11
23	15 000	2.4	17
35	22 000	5.4	39
76	48 000	25	187
103	65 000	46	340
126	79 000	69	520

Table 2
Imaging parameters used to tackle the range of spatial and temporal scales over the various fragmentation regimes explored. The symbols are the same ones used for Fig. 5 and 6. The conditions corresponding to ♦ (third line) are extracted from Machicoane et al. (2020). The same colors are used to represent the fields of view at scale in Fig. 2. (For interpretation of the references to color in this figure legend, the reader is referred to the web version of this article.)

Magnifications	Fields of view (mm^2)	dx (μm)	dt (ms)	Symbols
0.23	100 × 50	89	1	★
0.48	46 × 25	42	0.11	●
0.74	24 × 16	27	0.1	♦
1.1	14 × 11	18	0.09	■

Fig. 3 presents several snapshots at the conditions described in Table 1, covering the mentioned fragmentation regimes as the gas exit velocity is increased. Three out of the four fields of view are represented (lines 1 to 3 of Fig. 3 respectively), yielding different scales to appropriately measure the liquid core length. Note that the second smallest field of view (in red dashed line on Fig. 2) is not represented here as it corresponds to the four conditions sampled in Machicoane et al. (2020) (where the corresponding snapshots and movies are available; other conditions from that paper are not carried here as they considered the addition of angular momentum to the gas jet). In addition, five fragmentation regimes (non-axisymmetric Rayleigh–Plateau break-up, shear-break up without and with bag formation, and fiber-type atomization coexisting with bag break-up or not), represented in Fig. 3(c), (e), (f), (g), (i), and (j), have companion videos in the Supplementary Materials, illustrating the changes in temporal scales in addition to the one in spatial scales exhibited here.

3. Qualitative fragmentation regimes description and liquid core length analysis

The domains of existence of the fragmentation regimes are extracted qualitatively from the visualizations, to be used as guidelines of the a priori dominating physical break-up mechanisms. In addition, note that the non-linearity in the location of the different conditions when placed on the Weber number axis and the existence of transition

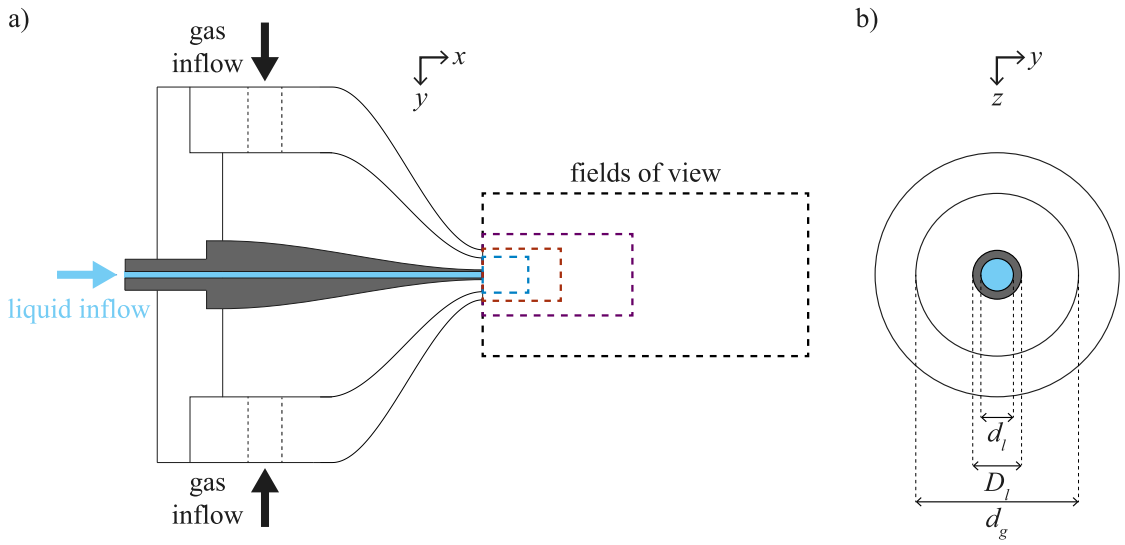

Fig. 2. (a) Longitudinal cut of the canonical two-fluid atomizer. The atomizer's axis is aligned with gravity and is only represented horizontally here for convenience. The liquid jet destabilization is imaged at larger and larger magnifications when the Weber is increased, yielding smaller and smaller fields of view indicated by dashed lines. (b) Transverse cut at the exit plane of the atomizer showing the liquid and gas diameters.

regions between two subsequent regimes contributes to blurring the lines distinguishing regimes. Up to $We_{d_l} = 1.7$, the liquid jet, while presenting shorter liquid core lengths, is fragmented in a manner that is qualitatively unaffected by the gas flow, and axisymmetric Rayleigh–Plateau break-up is observed. For $1.7 < We_{d_l} \leqslant 7.1$, deviations from axisymmetry place these conditions in the non-axisymmetric Rayleigh–Plateau break-up regimes. As illustrated in Fig. 3(d), the liquid jet is slightly meandering at $We_{d_l} = 7.1$ due to the possible onset of the shear instability caused by the difference in velocity between the gas and liquid phases. However, as break-up still happens similarly to that at lower Weber number values, i.e. resulting in typical drops and satellite droplets from a Rayleigh-type break-up, it is not classified as shear break-up regime, and may also be seen as a transitional value. Beyond this value, shear break-up occurs, yielding more polydisperse droplet size distributions. As bag (or membranes) start forming at the end of the liquid jet as early as for $We_{d_l} = 17$, the range of bag-less shear-break up is defined as $7.1 < We_{d_l} < 17$. At $We_{d_l} = 187$, while some bags can still be formed regularly, droplets are stripped from the liquid jet in fiber-type atomization, so bag break-up (without stripping) is observed for $17 \leqslant We_{d_l} < 187$. For $We_{d_l} \geq 520$, no bag formation is observed and only fiber-type atomization occurs.

Fig. 4(a) presents time series of the liquid core length L_B for three conditions in the non-axisymmetric Rayleigh–Plateau break-up, bag break-up, and fiber-type atomization regimes, respectively at $We_{d_l} = 7.1$, 40, and 340. The average value $\langle L_B \rangle$ is subtracted, and a division by the standard deviation L'_B is performed to center and normalize the signal. In addition, the conditions are shifted to be centered around 5, 0, and −5 respectively for clarity (the zero-mean level is added in dashed lines). The time axis is further normalized by the correlation timescale of the liquid core length τ_0 introduced in Machicoane et al. (2020) and further discussed below.

The time series are used to study either statistics or timescales of the liquid core length. For the former, the first three statistical moments are used, as the full statistics are faithfully represented by Skew-Normal distributions (Fig. 4(b)). This formalism is described in more detail in Kaczmarek et al. (2022); the function is defined as the product of a Gaussian and an error function, which depends only on three parameters directly expressed from the mean, standard deviation, and skewness of the signal. Skew-Normal distributions are displayed in dashed lines and show excellent agreement with the probability density functions (PDF) of the liquid core length. As the Weber number value increases, the PDF are shifted towards lower values of L_B and become narrower. This reveals a decrease of both the average and standard deviation, $\langle L_B \rangle$ and L'_B. The evolution of the third statistical moment, the skewness β_{L_B}, is not apparent here and will be discussed further in Section 4.

Auto-correlation functions of the liquid core length, defined as $R_{L_B}(\tau) = \langle L_B(t) L_B(t+\tau) \rangle / L'^2_B$ where τ is a time-lag, are computed to study the temporal dynamics (Fig. 4(c)). As the Weber number increases, faster decorrelation is observed. A liquid core length timescale τ_0 is extracted by computing the integral of the auto-correlation function up to 75% decorrelation, following Machicoane et al. (2020), i.e. $\tau_0 = \int_0^{\tau_T} R_{L_B}(\tau) d\tau$, with $R_{L_B}(\tau_T) = 0.25$.

4. Scaling laws of the liquid core length statistics and timescale

4.1. Gas Weber number representation

Fig. 5 presents the first three statistical moments of the liquid core length as functions of the gas Weber number. Note that since the liquid injection rate is constant and the two fluids in the experiments have constant physical properties, Weber number increases are simply obtained by increases of the gas exit velocity. The values at zero gas velocity are represented by black horizontal lines, as they are out of the range of Weber values presented here. The average liquid core length $\langle L_B \rangle$ has received considerable attention and is typically described as a power law of the gas-to-liquid dynamic pressure ratio M with an exponent −0.3 (see Leroux et al. (2007) for instance). Considering the small value of the liquid velocity here, $M^{-0.3}$ corresponds approximately to $We_{d_l}^{-0.3}$, at least in the range of high Weber numbers. This is in good agreement with what can be observed in Fig. 5(a) for $We_{d_l} \geqslant 39$, where a power-law fit of exponent -0.27 ± 0.04 is reported. This scaling is obtained as a best fit for $We_{d_l} \geqslant 85$, but the values found around $We_{d_l} = 39$ are also well captured by it. The scaling of the average liquid core length found at high Weber numbers, which is in good agreement with the literature, seems to apply only for a certain range of the bag-break-up regime and for fiber-type atomization. The lower range of bag-break ($17 \leqslant We_{d_l} < 39$), shear break-up, and Rayleigh–Plateau break-up regimes are not captured by this scaling and display a steeper decrease with the Weber number. Considering the definition chosen here, based on $U_g - U_l$, this lower range will be discussed further in terms of Re_g later on to better disentangle U_g and U_l (alternatively, plotting against M would be suitable, but since U_l

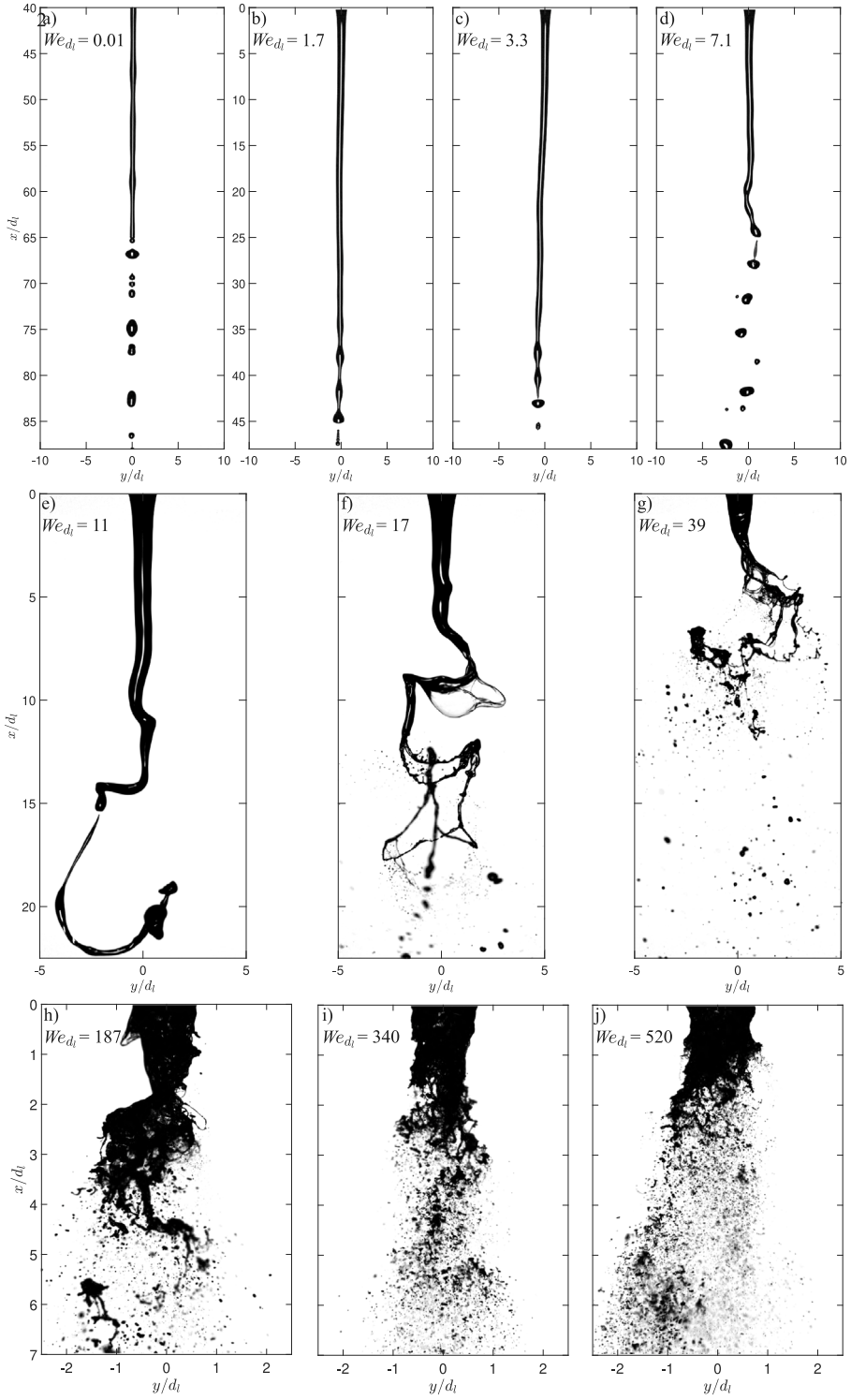

Fig. 3. Snapshots from high-speed back-lit imaging at different magnifications, highlighted by the growing apparent size of the liquid jet at the exit of the atomizer as the Weber number is increased from (a) to (i), where We_{d_l} is the gas Weber number based on the liquid jet inner diameter. (a–b) Axisymmetric Rayleigh–Plateau break-up; (c–d) Non-axisymmetric Rayleigh–Plateau break-up; Shear-break up without (e) and with bag formation (f–g); Fiber-type atomization, coexisting with bag break-up (h–i) or as a sole fragmentation regime (j); fragmentation regimes nomenclature from Lasheras and Hopfinger (2000).

is fixed, scaling found along $Re_g \sim U_g$ can be transposed in terms of $M \sim U_g^2$ straightforwardly).

While no scaling of L'_B is directly reported in the literature, some indications that the ratio $L'_B/\langle L_B \rangle$ should be constant exist (Kaczmarek et al., 2022). This is in agreement with the power law exponent −0.29 found here, with a 95% confidence interval on the fits' exponents that are twice the difference found between the exponent values found for the mean and standard deviation of the liquid core length. While more spread is associated with L'_B, the data is in agreement with the power law for Weber number values as low as $We_{d_l} = 3.3$. It then appears that this scaling applies even in the non-axisymmetric Rayleigh–Plateau break-up regime, while axisymmetric Rayleigh–Plateau break-up yields much higher values of L'_B (the values found at $We_{d_l} = 0.01$ and 1.7 are approximately 3 times larger than the value of L'_B for $We_{d_l} = 3.3$).

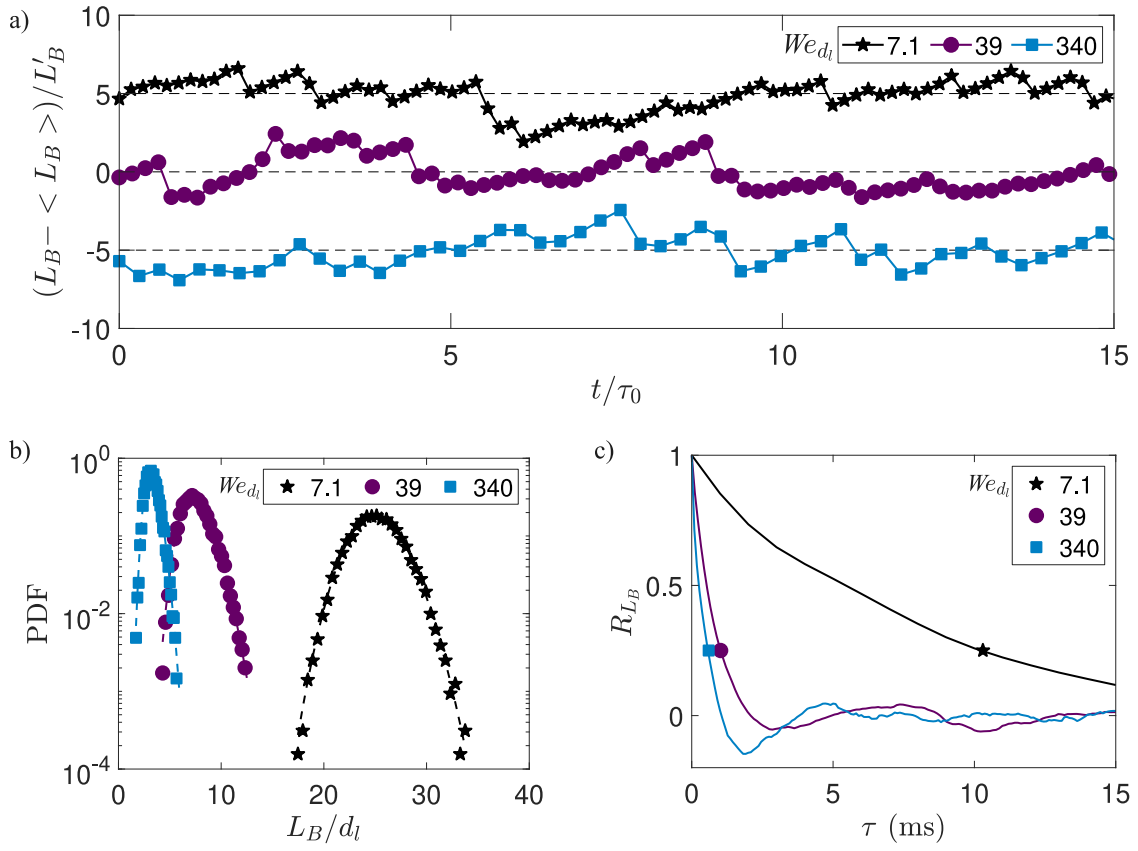

Fig. 4. (a) Time series of the centered and normalized liquid core length at three values of the gas Weber number. The black stars (★) and blue squares (■) are respectively shifted by 5 and −5 and black dash lines indicate the zero mean for all conditions. The time t is normalized by the liquid core length timescale τ_0. (b) Probability density functions of the liquid core length normalized by the liquid inner diameter, L_B/d_l. Dashed lines represent Skew-Normal distributions parametrized by the liquid core length mean, standard deviation, and skewness: $\langle L_B \rangle$, L'_B, and β_{L_B}. (c) Auto-correlation functions of the liquid core length R_{L_B} as a function of the time-lag τ. The symbols indicate decorrelation of 75% and a timescale τ_0 is calculated as the integral of the function up to that point. (For interpretation of the references to color in this figure legend, the reader is referred to the web version of this article.)

Similar to the standard deviation, the third-order statistical moment is associated with a larger spread. However, a plateau is found for high Weber numbers, with a positive skewness of $\beta_{L_B} = 0.46 \pm 0.09$. An increasing trend with We_{d_l} persists up to $We_{d_l} = 11$ (shear break-up regime), up to the asymptotic value. The spread prevents identification of whether this plateau is fully reached as early as $We_{d_l} = 17$ at the onset of bag break-up or if it is only truly attained for $We_{d_l} \geqslant 39$. One can also note that the skewness first decreases from the zero gas velocity case value when gas is added. Afterward, it increases monotonically and is first positive for $We_{d_l} = 7.1$.

In addition to the three statistical moments, the minimum value of the liquid core length is reported in Fig. 5(d). This is used as a proxy to what is referred to as the liquid cone length, by analogy to the potential cone in a turbulent round jet. This corresponds to the region where liquid is always present and is usually obtained through processing of average intensity maps from high-speed imaging. To avoid this image processing step that is not standardized among research groups, the liquid core length measurements are leveraged to estimate the cone length. The best fit for $We_{d_l} \geqslant 85$ reveals a power-law scaling with an exponent of −0.33, which is in good agreement with the decay of the first two statistical moments. At lower Weber number values, a steeper decrease following $We_{d_l}^{-0.89}$ is reported. Conditions in the vicinity of $We_{d_l} = 39$ seem to be in the transition between these regimes and are intersected by both fits. Note that while the decay of $\min(L_B)$ is approximately the same as $\langle L_B \rangle$ at high Weber numbers, it is approximately 1.5 times steeper in the lower range of values. The decay of the cone length at high Weber numbers is much less steep than the prediction made from conservation of mass flux argument resulting in $M^{-0.5}$ at high gas velocity (Lasheras and Hopfinger, 2000). A power law of exponent −0.5 is found in the intermediate range of Weber numbers, where moderate agreement could be argued within this restricted range. However, this range appears more likely to be a transition between power laws found at low and high Weber numbers.

4.2. Gas Reynolds number representation

The low range of gas velocities is observed for the average liquid core length in Fig. 6(a) as a function of the gas Reynolds number. A power law of exponent −0.54 is reported, equivalent to $M^{0.27}$. Power law of exponents −1 and −0.6 are also displayed in the low and high range of Reynolds number for comparisons. In the low range, the linear decrease underestimates the decay, which is found to follow $Re_g^{-1.23}$, but the scaling observed in the bag break-up regime remains fairly close to U_g^{-1}. The power law of exponent −0.6 corresponds to the scaling found by Leroux et al. (2007) with $M^{-0.3}$, and it is barely distinguishable from the best fit obtained in the high Reynolds numbers range. A power law of exponent −0.58 is found for the standard deviation of the liquid core length, indistinguishable from a $U_g^{-0.6}$ scaling in the explored range (not shown here). Fig. 6(b) display the absolute difference between the skewness of L_B and its asymptotic value at high Weber numbers, $\beta_{L_B}^{\infty} = 0.46 \pm 0.09$. The value 0.09, obtained as the standard deviation of the skewness values for $We_{d_l} > 39$, noted $\beta_{L_B}^{\infty\prime}$, is reported as a horizontal dashed line. A power-law fit with an exponent -2.34 ± 0.75 describes the decrease towards zero of $| \beta_{L_B} - \beta_{L_B}^{\infty} |$ as Re_g increases. The spread associated with this third-order statistical moment limits the accuracy in the determination of the exponent,

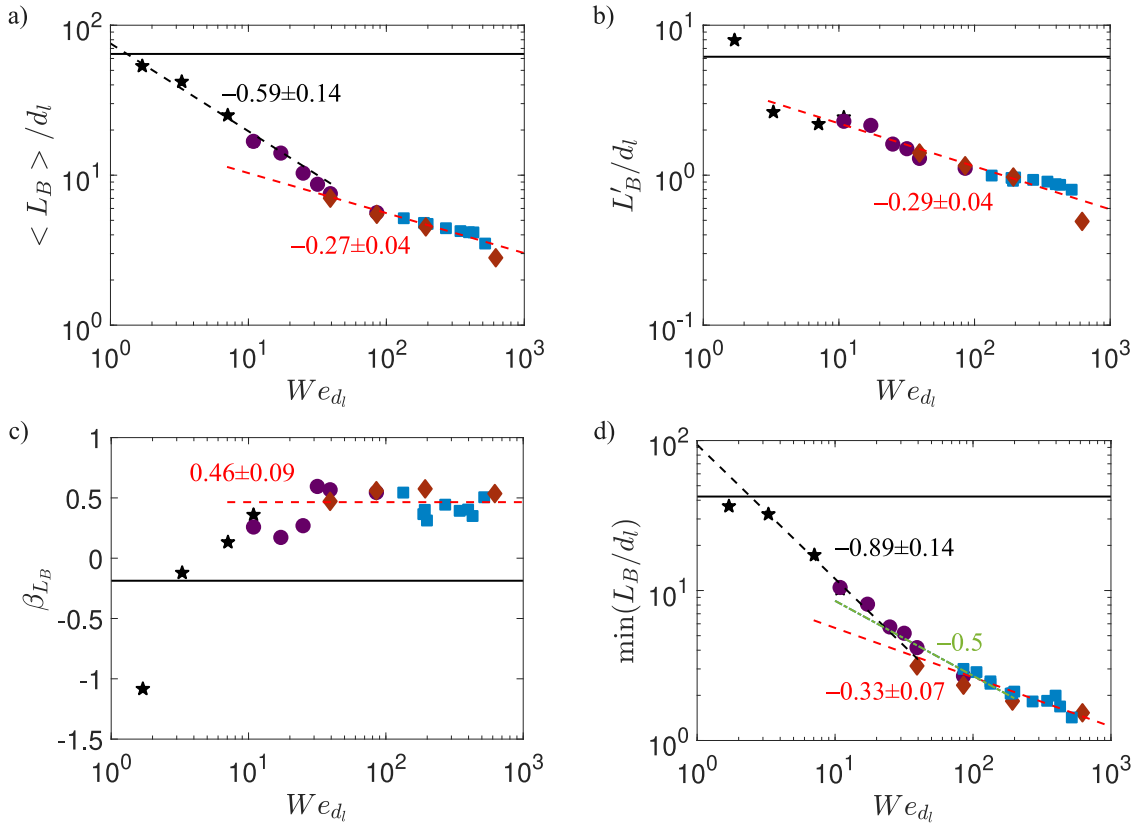

Fig. 5. Liquid core length mean (a), standard deviation (b), skewness (c), and minimum value (d): $\langle L_B \rangle$, L'_B, β_{L_B}, and $\min(L_B)$, normalized by the liquid inner diameter d_l and plotted along the gas Weber number based on the liquid jet inner diameter We_{d_l}. The black continuous lines indicate the values for $U_g = 0$. Black and red dashed lines in (a), (b), and (d) are power-law fits of the data in the low and high range of Weber numbers respectively. The adjacent values are the power-law exponents and their uncertainties, given by the 95% confidence intervals of the fits. A power law of exponent −0.5 is added as a green dash-dotted line in (d) to compare to the prediction from Lasheras and Hopfinger (2000). The values indicated around the red dashed line in (c) are the mean and standard deviation of the skewness values for $We_{d_l} > 39$. (For interpretation of the references to color in this figure legend, the reader is referred to the web version of this article.)

but the power-law fit seems to cross the value of 0.09 in the broad neighborhood of the transition to the bag break-up regime.

The timescale τ_0 extracted from the auto-correlation functions of the liquid core length is reported in Fig. 6(c–d) as a function of the gas Reynolds and Weber numbers respectively. At low gas velocity, this timescale is constant but smaller than in the absence of gas flow (approximately 5 ms versus the value of 11 ms at zero gas velocity). At the onset of the shear break-up regime, i.e. for $We_{d_l} \gtrsim 11$, a monotonic decrease is observed as the gas velocity increases. While the best fit found is a power law such as $We_{d_l}^{-0.61}$, equivalent to $Re_g^{-1.23}$, very good agreement is found with a linear decay, as attested by the dash-dotted line in Fig. 6(c).

5. Discussion

In addition to providing the scaling laws of the liquid core length statistics, timescale, and of the cone length, another objective of this paper is to infer a quantitative framework that indicates transitions between fragmentation regimes. Axisymmetric Rayleigh–Plateau break-up is characterized by very high values of the liquid core length standard deviation L'_B, that deviate strongly from the scaling $We_{d_l}^{-0.3}$ (alternatively $M^{-0.3}$ as reported in the literature for the average value, e.g. Leroux et al. (2007)) found for other regimes. In addition, it is associated with negative skewness values β_{L_B}. However, a negative value, although close to 0, has been displayed for a condition in the non-axisymmetric Rayleigh–Plateau break-up regime, so this may not be a discriminatory criterion. It requires much more converged statistics to be employed. The transition to this regime can be identified as the Weber number value at which the power law of exponent −0.3 is met, $We_{d_l} = 3.3$ here.

Shear break-up occurs when the velocity difference between both phases is large enough to trigger a large-scale shear instability that results in the back-and-forth motions of the liquid jet called flapping. In this regime, the liquid jet dynamics are closely linked to the gas jet, and the flapping frequency is simply proportional to the gas jet's mean exit velocity (Delon et al., 2018). The liquid core length timescale τ_0 is observed to approximately decrease linearly with the gas velocity at the onset of the shear break-up regime. Before that, τ_0 is found at much higher values and no dependency on the gas velocity is found. This constant value is approximately twice smaller than in the absence of the gas flow. In the shear break-up regime and beyond, the gas jet exit velocity is found to drive the timescale of the liquid jet proportionally. The shear break-up is therefore identified to start at $We_{d_l} = 11$.

The onset of bag formation does not appear to affect the metrics reported here in an evident way. It may have a signature on the skewness of the liquid core length, as the average behavior towards the asymptotic value, exhibited by the power-law fit in Fig. 6(b), seems to approach the neighborhood of $\beta^{\infty'}_{L_B}$ in the vicinity of the transition to the bag break-up regime. The asymptotic value may, however, be reached at slightly higher Weber number values. A tighter sampling of operating conditions with an increased number of realizations would be necessary to confirm this suspected behavior, though. In addition, when investigating the flapping of the liquid jet, a transition from meandering motions in a plane to 3D quasi-circular orbits is observed for $We_{d_l} \gtrsim 39$ (Kaczmarek et al., 2022). Below this transition, bags are only formed at the end of the liquid jet, in the hook-like shapes formed by the meandering motion. While small droplets are produced

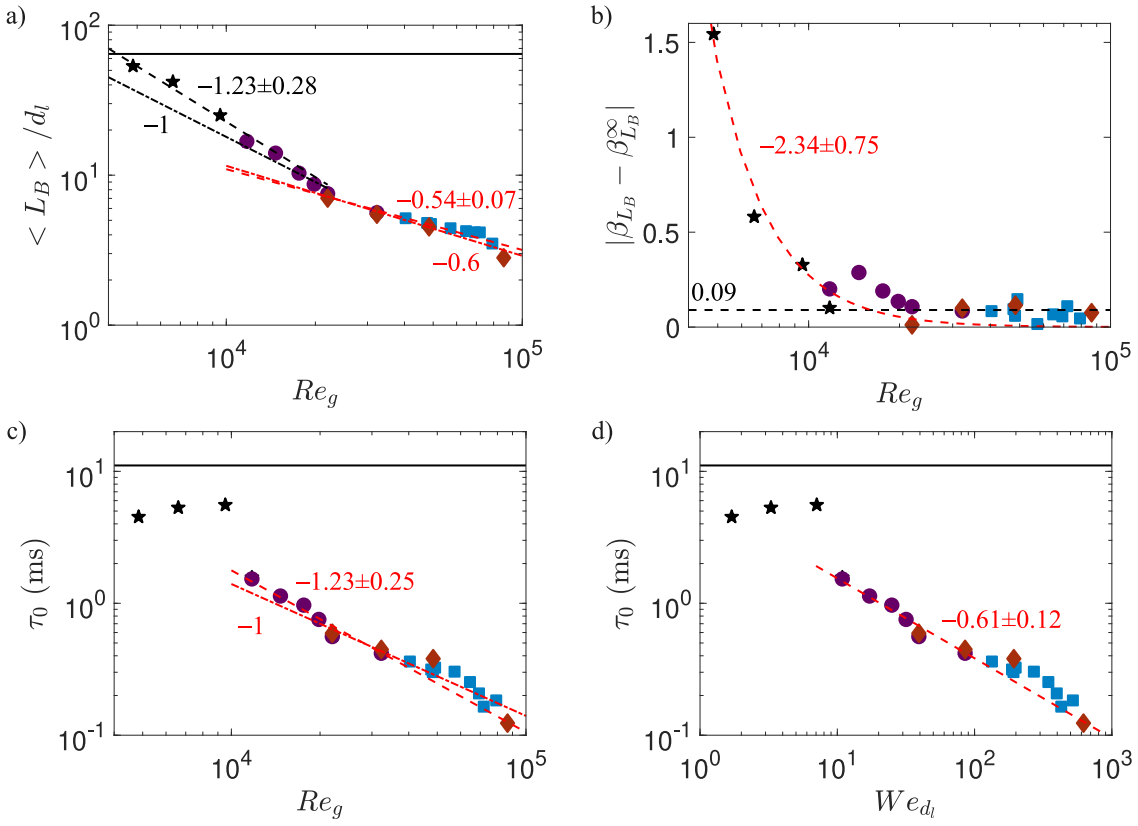

Fig. 6. Normalized liquid core length mean (a), absolute difference between the skewness and its high We_{d_l} asymptotic value (b), and liquid core length timescale (c): $\langle L_B/d_l \rangle$, $|\beta_{L_B} - \beta^{\infty}_{L_B}|$, τ_0, plotted along the gas Reynolds number Re_g. (d) τ_0 plotted along the gas Weber number based on the liquid jet inner diameter We_{d_l}. The black continuous lines indicate the values for $U_g = 0$. Dash-dotted lines in (a) and (c) represent power laws whose exponents are indicated along with their uncertainties, given by the 95% confidence intervals of the fits. The black dashed line in (b) is the standard deviation of the skewness values for $We_{d_l} > 39$, while the red dashed line represents a fit of the growth towards the asymptotic value $\beta^{\infty}_{L_B}$. (For interpretation of the references to color in this figure legend, the reader is referred to the web version of this article.)

by the break-up of these bags, the dynamics of the liquid jet remain the same. After this transition, in addition to the large-scale shear instability, localized Kelvin–Helmholtz instabilities result in small-scale perturbations, which are elongated by the gas flow and can form bags on the side of the liquid jet. In this case, the flapping characteristics are heavily affected, and the region in the vicinity of the atomizer's exit plane becomes much more populated with droplets. This regime, which is termed "KH-bag break-up" (while the regime where bags only occurs at the end of the liquid jet can be termed "flapping-bag break-up"), where several bags can be formed at the same time along the liquid jet. This regime leads to a drastic increase in break-up events and could be seen as the start of atomization, as liquid is being stripped simultaneously from the liquid jet at multiple locations. A movie is provided at $We_{d_l} = 39$ in the Supplementary Material to illustrate KH-bag break-up. It differs from fiber-type atomization in the sense that the local interfacial perturbations are not accelerated enough by the gas jet to suffer from Rayleigh–Taylor instabilities, so no small ligaments or droplets are directly peeled off the liquid jet. The onset of KH bags is marked by the onset of power laws of exponent −0.3 for $We_{d_l} \geq 39$ for the mean and minimum value of the liquid core length. This change in scaling laws seems to reveal the onset of localized Kelvin–Helmholtz instabilities, in the same way that the onset of the shear instability is associated with a change in the behavior of τ_0.

The transition to fiber-type atomization occurs for $We_{d_l} \geqslant 187$, where it coexists with the formation of KH bags until $We_{d_l} = 340$. No change in the scaling laws of the reported metrics is observed around this transition. However, at smaller scales, it was reported to affect the scaling of the transport of interfacial perturbations (Ricard et al., 2021). Before this transition (i.e. $We_{d_l} \leq 187$), the spatial growth rate of the mean velocity of interfacial perturbations follows U_g^2, while it increases linearly with the gas velocity after the transition. The end of the occurrence of bag formation leaves no signature either. In addition, at very high gas Weber numbers, the gas flow is observed to recirculate behind the liquid, forming a hollow liquid core, termed liquid crown due to the crenelation-shaped structures formed by the ligaments peeled off from the rim of the hollow liquid core (Machicoane et al., 2019). This occurs for $We_{d_l} \geqslant 620$ and is only observed for one condition, so no conclusion can be drawn about this regime. It may be associated with the drop in standard deviation of the liquid core length in Fig. 5(b), but exploring the behavior of L_B at higher Weber number values would be necessary to confirm this. The quantitative indicators that best highlight the signature of the transitions among the fragmentation regimes discussed here are summarized in Table 3.

6. Conclusions

A coaxial two-fluid atomizer is used to study the gas-assisted fragmentation of a liquid jet over three decades of gas Weber number, which compares the aerodynamic stresses to the liquid jet's surface tension force. This range spans the axisymmetric Rayleigh–Plateau break-up, non-axisymmetric Rayleigh–Plateau break-up, shear break-up with and without bag formation, and fiber-type atomization regimes as the Weber number increases. The study focuses on the liquid core length statistics and temporal dynamics, as time series are extracted from back-lit high-speed imaging. Scaling laws with respect to the gas Reynolds number Re_g and the gas Weber number We_{d_l} are obtained for the mean, standard deviation, skewness, minimum value, and correlation time of the liquid core length.

The changes in scaling laws with respect to the governing non-dimensional numbers appear to be able to serve as a quantitative

Table 3
Proposed quantitative indicator for the onset of the different fragmentation regime identified for a laminar liquid jet surrounded by a gas jet. $\langle L_B \rangle$, $\min(L_B)$, and L'_B are the average, minimum value and standard deviation of the liquid core length L_B, while τ_0 is its correlation time.

Onset of	Indicator
Non-axisymmetric Rayleigh–Plateau break-up	L'_B
Shear break-up	τ_0
Shear break-up with bags	No indicator found
Shear break-up with Kelvin–Helmholtz bags	$\langle L_B \rangle$, $\min(L_B)$, and flapping (Kaczmarek et al., 2022)
Fiber-type atomization with bags	Transport of interfacial perturbations (Ricard et al., 2021)
Fiber-type atomization without bags	No indicator found

indicator of the transitions between fragmentation regimes. The standard deviation of the liquid core length L'_B is found to follow a power-law decay, with the same exponent as reported for the average value in the literature and found here, as early as the onset of the non-axisymmetric Rayleigh–Plateau break-up regime. For lower Weber numbers values, L'_B is found at much higher values, marking a clear quantitative transition. Similarly, the onset of the shear break-up regime is indicated by the shift of the correlation time from constant high values to a linear decay. The transition to the start of the bag break-up regime is less clearly identified but could potentially have a signature on the skewness. However, the transition to what is here referred to as the KH-bag break-up regime, where bags can form on the side of the liquid jet and not only on its end, is marked by the mean and minimum value of L_B reaching the power law of exponent -0.3. In this regime, localized Kelvin–Helmholtz instabilities yield small-scale perturbations close to the atomizer exit plane that can form bags, and flapping is no longer happening in 2D meandering motions. These scaling laws and behaviors will be confirmed in future work considering variations of the liquid exit velocity, to properly identify relevant non-dimensionless groups. Finding quantitative indicators for the onset of bags in the shear break-up regime as well as for the disappearance of bags in fiber-type atomization remain open questions.

CRediT authorship contribution statement

Nathanaël Machicoane: Conceptualization, Methodology, Formal analysis, Investigation, Writing – original draft. **Rodrigo Osuna-Orozco:** Investigation, Writing – review & editing. **Alberto Aliseda:** Writing – review & editing, Funding acquisition.

Declaration of competing interest

The authors declare that they have no known competing financial interests or personal relationships that could have appeared to influence the work reported in this paper.

Data availability

Data will be made available on request.

Acknowledgments

This work was sponsored by the Office of Naval Research (ONR), USA as part of the Multidisciplinary University Research Initiatives (MURI) Program, under grant number N00014-16-1-2617. The views and conclusions contained herein are those of the authors only and should not be interpreted as representing those of ONR, the U.S. Navy or the U.S. Government.

Appendix A. Supplementary data

Supplementary material related to this article can be found online at https://doi.org/10.1016/j.ijmultiphaseflow.2023.104475.

References

Aliseda, A., Hopfinger, E., Lasheras, J.C., Kremer, D., Berchielli, A., Connolly, E., 2008. Atomization of viscous and non-Newtonian liquids by a coaxial, high-speed gas jet. Experiments and droplet size modeling. Int. J. Multiph. Flow. 34 (2), 161–175.

Charalampous, G., Hadjiyiannis, C., Hardalupas, Y., 2019. Proper orthogonal decomposition of primary breakup and spray in co-axial airblast atomizers. Phys. Fluids 31 (4), 043304. http://dx.doi.org/10.1063/1.5085416.

Charalampous, G., Hardalupas, Y., Taylor, A., 2009. Structure of the continuous liquid jet core during coaxial air-blast atomisation. Int. J. Spray Combust. Dyn. 1 (4), 389–415.

Chigier, N., Farago, Z., 1992. Morphological classification of disintegration of round liquid jets in a coaxial air stream. At. Spray. 2 (2).

Clanet, C., Lasheras, J.C., 1999. Transition from dripping to jetting. J. Fluid Mech. 383, 307–326.

Delon, A., Cartellier, A., Matas, J.-P., 2018. Flapping instability of a liquid jet. Phys. Rev. Fluids 3 (4), 043901.

Dumouchel, C., 2008. On the experimental investigation on primary atomization of liquid streams. Exp. Fluids 45 (3), 371–422.

Eroglu, H., Chigier, N., Farago, Z., 1991. Coaxial atomizer liquid intact lengths. Phys. Fluids A Fluid Dyn. 3 (2), 303–308.

Fong, K.O., Xue, X., Osuna-Orozco, R., Aliseda, A., 2022. Two-fluid coaxial atomization in a high-pressure environment. J. Fluid Mech. 946.

Huck, P., Osuna-Orozco, R., Machicoane, N., Aliseda, A., 2022. Spray dispersion regimes following atomization in a turbulent co-axial gas jet. J. Fluid Mech. 932, http://dx.doi.org/10.1017/jfm.2021.992.

Juniper, M.P., Candel, S.M., 2003. The stability of ducted compound flows and consequences for the geometry of coaxial injectors. J. Fluid Mech. 482, 257–269.

Kaczmarek, M., Osuna-Orozco, R., Huck, P.D., Aliseda, A., Machicoane, N., 2022. Spatial characterization of the flapping instability of a laminar liquid jet fragmented by a swirled gas co-flow. Int. J. Multiph. Flow. 152, 104056. http://dx.doi.org/10.1016/j.ijmultiphaseflow.2022.104056, URL https://www.sciencedirect.com/science/article/pii/S0301932222000672.

Kumar, A., Sahu, S., 2018. Liquid jet breakup unsteadiness in a coaxial air-blast atomizer. Int. J. Spray Combust. Dyn. 10 (3), 211–230. http://dx.doi.org/10.1177/1756827718760905.

Kumar, A., Sahu, S., 2020. Influence of nozzle geometry on primary and large-scale instabilities in coaxial injectors. Chem. Eng. Sci. 221, 115694.

Lasheras, J.C., Hopfinger, E., 2000. Liquid jet instability and atomization in a coaxial gas stream. Annu. Rev. Fluid Mech. 32 (1), 275–308.

Leroux, B., Delabroy, O., Lacas, F., 2007. Experimental study of coaxial atomizers scaling. Part I: dense core zone. At. Spray. 17 (5).

Machicoane, N., Bothell, J.K., Li, D., Morgan, T.B., Heindel, T.J., Kastengren, A.L., Aliseda, A., 2019. Synchrotron radiography characterization of the liquid core dynamics in a canonical two-fluid coaxial atomizer. Int. J. Multiph. Flow. 115, 1–8. http://dx.doi.org/10.1016/j.ijmultiphaseflow.2019.03.006.

Machicoane, N., Ricard, G., Osuna-Orozco, R., Huck, P.D., Aliseda, A., 2020. Influence of steady and oscillating swirl on the near-field spray characteristics in a two-fluid coaxial atomizer. Int. J. Multiph. Flow. 129, 103318. http://dx.doi.org/10.1016/j.ijmultiphaseflow.2020.103318.

Marmottant, P., Villermaux, E., 2004. On spray formation. J. Fluid Mech. 498, 73–111.

Matas, J.-P., Delon, A., Cartellier, A., 2018. Shear instability of an axisymmetric air–water coaxial jet. J. Fluid Mech. 843, 575–600.

Mayer, W., Branam, R., 2004. Atomization characteristics on the surface of a round liquid jet. Exp. Fluids 36 (4), 528–539.

Osuna-Orozco, R., Machicoane, N., Huck, P.D., Aliseda, A., 2022. Effect of electrostatic forcing on coaxial two-fluid atomization. Phys. Rev. Fluids 7 (7), 074301. http://dx.doi.org/10.1103/PhysRevFluids.7.074301.

Ricard, G., Machicoane, N., Osuna-Orozco, R., Huck, P.D., Aliseda, A., 2021. Role of convective acceleration in the interfacial instability of liquid-gas coaxial jets. Phys. Rev. Fluids 6 (8), 084302. http://dx.doi.org/10.1103/PhysRevFluids.6.084302.

Singh, G., Jayanandan, K., Kourmatzis, A., Masri, A., 2021. Spray atomization and links to flame stability over a range of Weber numbers and pressure ratios. Energy Fuels 35 (19), 16115–16127.
Varga, C.M., Lasheras, J.C., Hopfinger, E.J., 2003. Initial breakup of a small-diameter liquid jet by a high-speed gas stream. J. Fluid Mech. 497, 405–434.
Villermaux, E., 2007. Fragmentation. Annu. Rev. Fluid Mech. 39, 419–446.
Zhao, H., Liu, H.-F., Tian, X.-S., Xu, J.-L., Li, W.-F., Lin, K.-F., 2014. Influence of atomizer exit area ratio on the breakup morphology of coaxial air and round water jets. AIChE J. 60 (6), 2335–2345.